Materials Science in Semiconductor Processing 40 (2015) 943–953

Contents lists available at ScienceDirect

Materials Science in Semiconductor Processing

journal homepage: www.elsevier.com/locate/mssp

Morphology and defect evolution in vapor-grown In_2O_3:Sn micro-/nanoparticles

Jesús Alberto Ramos Ramón [a], Diego León Sánchez [b], Manuel Herrera Zaldívar [c], Umapada Pal [a,*]

[a] Instituto de Física, Benemérita Universidad Autónoma de Puebla, Apdo. Postal J-48, Puebla 72570, Mexico
[b] Facultad de Ciencias de la Electrónica, Universidad Autónoma de Puebla, 18 Sur y Av. San Claudio, Edif. 109, Puebla, Pue. 72570, Mexico
[c] Centro de Nanociencia y Nanotecnología, Universidad Nacional Autónoma de México, km 107 Carretera Tijuana-Ensenada, Ensenada, B.C. 22800, Mexico

ARTICLE INFO

Article history:
Received 13 May 2015
Received in revised form
9 August 2015
Accepted 9 August 2015

Keywords:
Indium oxide
Micro- and nanoparticles
Tin doping
Raman spectroscopy
Cathodoluminescence

ABSTRACT

Sn-doped indium oxide micro- and nanoparticles with different Sn contents (0–15 wt% nominal) were grown by vapor-transport method. Effects of Sn content on the morphology and defect evolution in the crystalline particles were studied using scanning electron microscopy, micro-Raman, cathodoluminescence (CL), and UV–vis optical absorption spectroscopy techniques. It has been observed that Sn doping enhances the direct band gap energy of In_2O_3 micro-/nanostructures, modifies their morphology and electronic defect structures. By controlling the concentration of Sn, CL emission behavior of In_2O_3 nanostructures can be controlled systematically.

1. Introduction

Indium oxide (In_2O_3) is a semiconducting metal oxide, which has been actively studied due to its potential technological applications in sensors [1–3], display devices [4,5], catalysts [6,7], and solar cells [8,9]. While In_2O_3 itself is highly transparent in the UV–vis spectral region due to wide band gap energy ($Eg \approx 3.6$ eV) [10], to enhance electrical conductivity, often it has been doped with metals such as Sn [5,11], and Zn [12–14]. The high electrical conductivity of these doped In_2O_3 is associated to the high mobility of charge carriers, principally the electrons in these n-type semiconductors. Due to excellent optical transparency and adequate electrical conductivity, doped In_2O_3 thin films have been utilized as efficient transparent conducting electrodes in several optoelectronic devices. For example, Sn-doped indium oxide (also known as ITO) has been widely used for optoelectronic applications, such as anode material in organic light emitting diodes (OLEDs) [15], transparent heat mirrors for aircraft and car windows [16], and photovoltaic devices [17]. On the other hand, nanostructures of these metal oxides have shown to be very promising for chemical sensing due to their large surface area and presence of oxygen vacancies in high concentrations [18]. Due to high surface-to-volume ratio, In_2O_3 based nanomaterials are better suited for chemical sensing. Apart from surface area, morphology and impurity content in these nanostructures have seen to control their effectiveness in several applications. For example, undoped In_2O_3 nanostructures of pyramid shape, one dimensional nanowire or nanorods, and nanotubes of In_2O_3 have seen to be effective as field emission device [19], chemical sensor [20], and toxic gas detectors [21–23], respectively. In fact, fabrication of inorganic nanostructures with specific morphology is required to meet different scientific and technological needs. Using different techniques, such as spray pyrolysis [22], sputtering [15], metal-organic chemical vapor deposition [23], vapor–liquid–solid growth [24], hydrothermal process [25], and sol–gel [26], nanostructures of indium oxide and indium tin oxide of different morphologies such as nanoparticles [26], nanoellipses [27], nanowires [28,29], nanorods [27], and nanofibers [30], have been successfully fabricated. Well-shaped nanoparticles of In_2O_3 and ITO have been fabricated by direct heating of indium metal [31] and indium/In_2O_3 mixture [32], respectively. While the low-dimensional tin oxide and ITOs have been fabricated widely in thin film form and applied successfully in sensing and optoelectronic devices, in nanostructure form, they are promising for the fabrication of devices with higher efficiency at lower costs as compared to thin film devices [33]. However, nanostructures of indium oxide or indium tin oxide have received less attention and need further investigation for their technological applications.

* Corresponding author.
E-mail address: upal@ifuap.buap.mx (U. Pal).

http://dx.doi.org/10.1016/j.mssp.2015.08.021
1369-8001/

In the present work, we fabricated In_2O_3 and Sn-doped In_2O_3 micro- and nanoparticles through vapor–solid (VS) growth process, to study the effect of Sn incorporation on their morphology and optical properties. Scanning electron microscopy (SEM) and energy-dispersive X-ray spectroscopy (EDS) techniques were used to analyze the morphology and composition of the nanostructures prepared with different Sn contents (0–15 wt% nominal). UV–vis spectroscopy and cathodoluminescence (CL) spectroscopy have been used to study

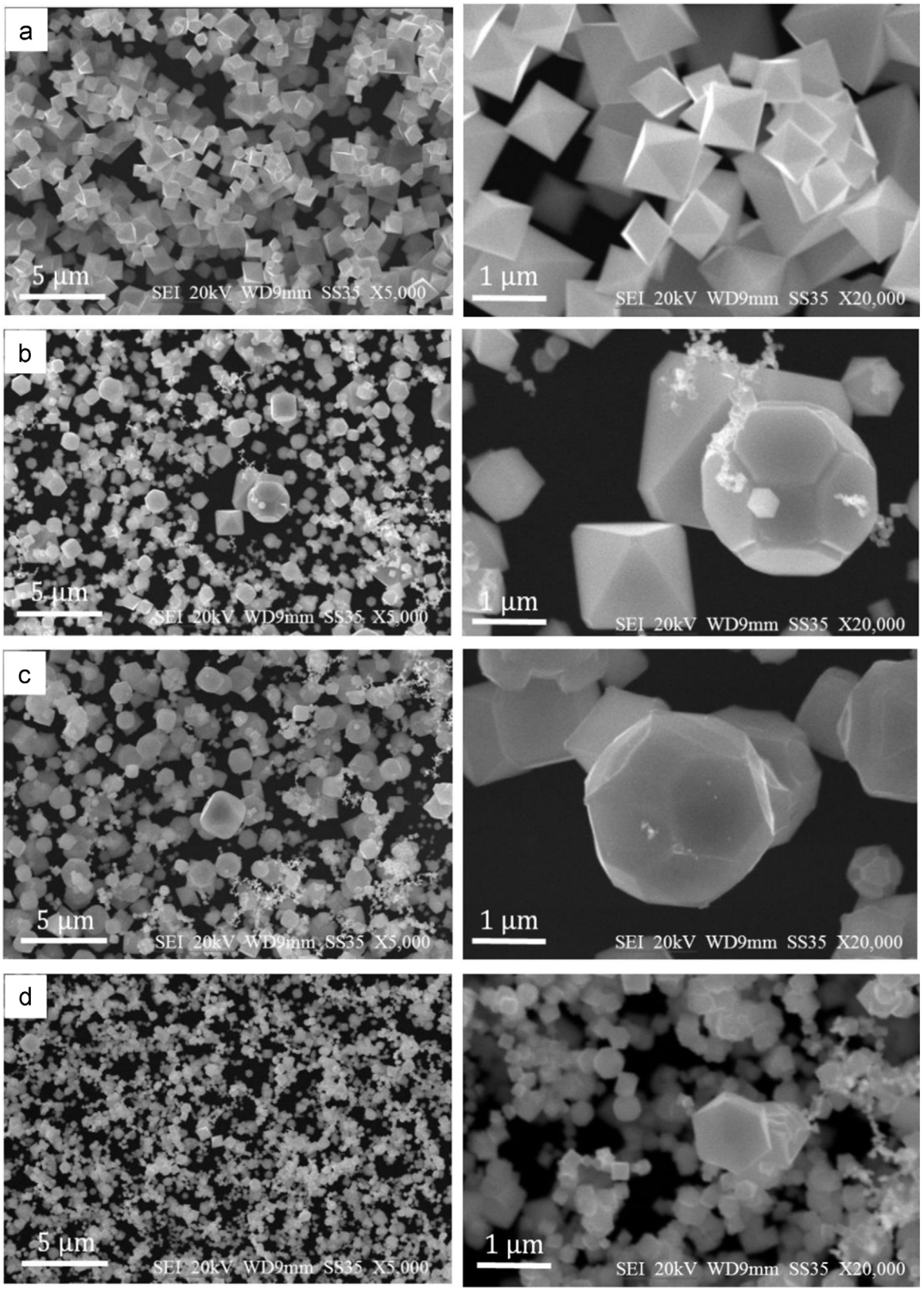

Fig. 1. Typical SEM images of the In_2O_3 nanoparticles containing (a) 0.0, (b) 5.0, (c) 10.0, and (d) 15.0 wt% (nominal) of Sn. Images taken at higher magnification are shown in the right column beside the low magnification image of the corresponding sample.

their optical properties and emission behaviors. Room temperature micro-Raman spectroscopy technique was utilized to monitor the changes occurred in In_2O_3 lattice by Sn doping.

2. Experimental

Undoped and Sn-doped indium oxide micro- and nanoparticles were grown by vapor-transport deposition process in a single-zone high-temperature tube furnace, equipped with flow control system. In metal and In–Sn alloys of different compositions were used as precursors. In–Sn alloys of different Sn contents were prepared by heating the mixtures of indium and tin of 100:*X* (*X*=5, 10 and 15) weight ratios at 520 °C for 8 h in a close horizontal furnace under Ar atmosphere. Alloys obtained by this way were mixed with graphite powder in 4:1 weight ratio, and put into an alumina boat as source material. The alumina boat was then placed at the center of a quartz tube (2 cm inner diameter and 120 cm length), and inserted into the tube furnace at room temperature. Before heating, high purity Ar gas (99.996%) was passed through the quartz tube for about 30 min. A quartz substrate was placed at about 15 cm downstream of the source material. The temperature of the furnace and hence the precursor in the alumina boat was raised to 1100 °C by heating at the rate of 30 °C/min under constant flow (220 sccm) of $Ar+O_2$ gas mixture (10:1 v/v). At this temperature of the precursor mixture, the substrate temperature was about 700 °C. After maintaining the maximum temperature at 1100 °C for 2 h, the furnace was cooled down to room temperature. For the synthesis of undoped indium oxide nanoparticles, a mixture of In and graphite powder (4:1 w/w) was put into the alumina boat and the growth was performed under the same earlier mentioned experimental conditions. The nano-/microstructures deposited over quartz substrates were collected for characterized using different techniques. A JEOL JSM-6610 scanning electron microscope (SEM) with attached Oxford analytical system was used to study the morphology and composition of the undoped and doped nanoparticles. Room temperature Raman spectra of the samples were recorded under 632.8 nm excitation from a He–Ne laser in a Horiba JOBIN-YVON spectrophotometer fitted with a charge coupled detector. For optical characterization, the absorption spectra of the samples were recorded in the 200–800 nm spectral range using a UV–vis spectrophotometer (SHIMADZU UV-3101PC). Cathodoluminescence (CL) spectra of the doped and undoped samples were recorded in a JEOL JIB-4500 scanning electron microscope fitted with a Gatan mono-CL4 system at room temperature and at 100 K.

3. Results and discussion

Fig. 1 shows typical SEM images of In_2O_3 and In_2O_3:Sn structures grown by vapor transport process. As can be seen, Sn incorporation

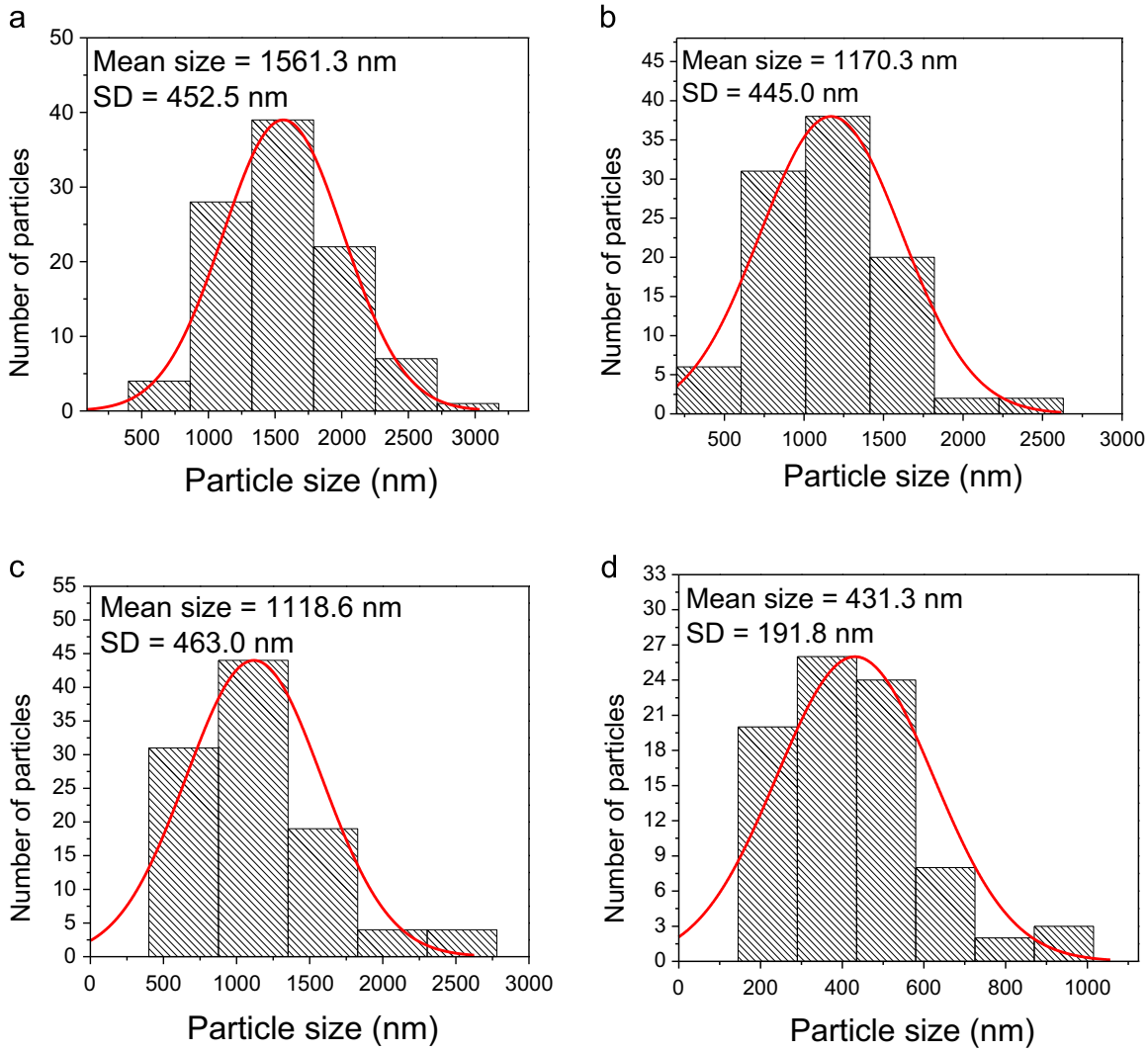

Fig. 2. Size distribution histograms and corresponding Gaussian fits for the (a) undoped, (b) 5.0, (c) 10.0, and (d) 15.0 wt% (nominal) Sn-doped In_2O_3 nanoparticles.

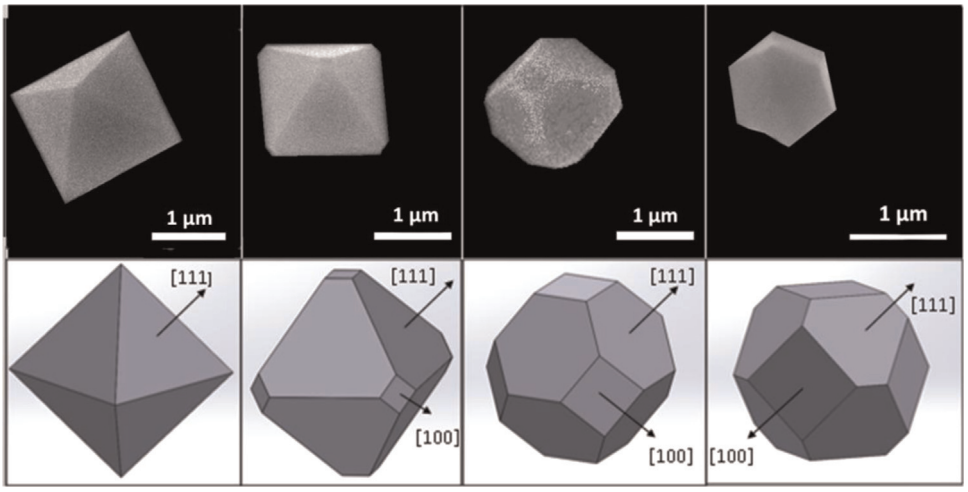

Fig. 3. Typical shapes of the vapor grown In_2O_3 particles containing (a) 0.0, (b) 5.0, (c) 10.0, and (d) 15.0 wt% (nominal) Sn, and their corresponding schematic structures (lower row). The surface energy of (111) planes becomes higher than the energy of (100) planes on Sn incorporation, and the morphology of particles changes from octahedron to truncated-octahedron.

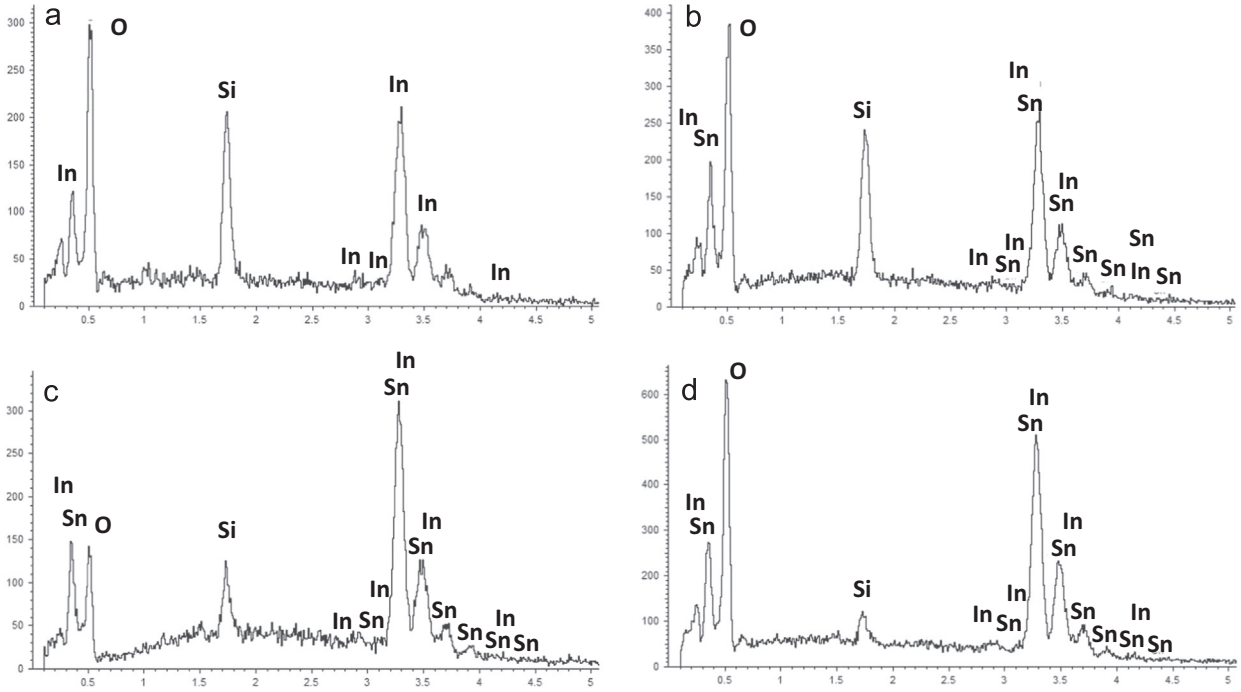

Fig. 4. EDS spectra of the (a) undoped, (b) 5.0 wt %, (c) 10.0 wt%, and (d) 15.0 wt% (nominal) Sn-doped In_2O_3 samples. The Si peak appeared from the Si substrate used to disperse the samples for SEM/EDS analysis.

severely affects the morphology of the structures. While the undoped indium oxide structures were grown in well-defined octahedral shape with about 1561 nm average size, on incorporating Sn, their morphology changed from octahedral to faceted octahedral and semispherical shapes with a gradual size reduction. The change of average size of these micrometric and sub-micrometric structures with the increase of Sn content can be clearly perceived from the size distribution histograms presented in Fig. 2. Sn incorporation in In_2O_3 increases the root mean square micro strain, increasing lattice defects and gradually reducing particle size on increasing Sn content [26]. For Sn-doped indium oxide in its common bcc structure, the surface energy (γ) relationship among the low-index crystallographic planes should be $\gamma\{111\} < \gamma\{100\} < \gamma\{110\}$[32, 34]. As the growth rates (r) normal to different crystal planes are proportional to their surface energies, their ratios define the final shape of the grown nanocrystals. While for $r\{100\}/r\{111\} \approx 1.73$, we should expect a perfect octahedral shape for ITO nano-/microparticles, for $0.87 \leq r\{100\}/r\{111\} \leq 1.73$, formation of truncated octahedrons would be expected [32]. On incorporation of Sn in In_2O_3, the surface energy of its crystal planes and hence the ratio of their growth rates changes, resulting a change in the final morphology of nanocrystals. However, any change in growth conditions such as fluctuation of growth temperature or the flow rate of carrier gas in vapor growth process may also affect the chemical potentials of different crystallographic planes, resulting in the change of growth rate of different crystallographic planes [35,36]. With the variation of Sn content, both the morphology and size of the In_2O_3 micro-/nanostructures changed drastically (Fig. 1). The evolution of morphology can be followed if we consider the bigger particles in each of the samples. Fig. 3 presents the typical morphologies of the micro-/nanostructures formed in the samples prepared with different Sn contents in the precursors. As can be seen, incorporation

Table 1
EDS estimated elemental quantification of Sn-doped In_2O_3 samples.

Sample	Element	At%
In_2O_3	In	39.02
	O	60.98
In_2O_3:Sn 5%	In	33.47
	O	64.30
	Sn	2.22
In_2O_3:Sn 10%	In	31.24
	O	66.42
	Sn	2.35
In_2O_3:Sn 15%	In	30.10
	O	67.40
	Sn	2.50

of Sn induces facets, transforming octahedral particles to truncated octahedral shapes. Non-uniform morphology of the micro-/nanostructures (Fig. 1) revealed in the Sn-doped In_2O_3 samples is also expected due to the difference between the vapor pressures of In and Sn in the alloy precursors, which induces inhomogeneous evaporation of the elements during heating. The vapor pressures of In and Sn at 1100 °C are 207 mTorr and 0.95 mTorr, respectively [37]. This might also be the reason of the lower (than the nominal value) Sn content in Sn-doped samples estimated from their EDS analysis (Fig. 4 and Table 1). However, the Sn incorporation in the micro-/nanostructures is quite homogeneous. Homogeneous distribution of In, O, and Sn in Sn-doped micro-/nanostructures can be perceived in their elemental mapped images presented in Figs. 5, 6 and 7.

As presented in Table 1, the Sn content in the samples increases with the increase of nominal Sn content in the precursors. The In: O atom % ratio in the samples varied from 0.64 to 0.45, revealing high oxygen excess in all the micro-/nanostructures due to adsorption of O_2 in the growth process in the quartz tube [38], and from other sources as discussed later.

Room temperature Raman spectra of the undoped and Sn-doped indium oxide samples were recorded in the 100–800 cm^{-1} spectral range (Fig. 8). Cubic In_2O_3 belongs to space group I_a^3 (T_h^7) having 22 Raman active modes (A_g, E_g and T_g symmetry) and 16 infrared active modes (T_u symmetry). A few vibrations such as A_u and E_u are inactive in both infrared and Raman [23,39]. The Raman spectrum of our In_2O_3 micro-/nanoparticles revealed 10 vibrational modes, located at about 111, 118, 134, 154, 308, 368, 431, 496, 629 and 709 cm^{-1}. While the bands around 111, 154, 308, 368, and 629 cm^{-1} have T_g symmetry, the bands at 134, and 496 cm^{-1} have A_g symmetry. The vibrational modes at 119 and 429 cm^{-1} correspond to in-plane vibrations of terminal oxygen and stretching mode of the rhombus oxygen atoms of the In_2O_3 cluster [40], as presented in Fig. 9. The vibrational mode appeared around 707 cm^{-1} has also been observed by White et al. [41], and Kim et al. [42] and been assigned exclusively to the cubic phase of In_2O_3. Raman spectra of the Sn-doped samples revealed all the Raman bands of undoped sample (Fig. 8), indicating that the main contribution to the vibrational modes comes from the In_2O_3 host lattice [39]. However, Sn doping in In_2O_3 affects both the intensity and position of its vibrational modes. On Sn incorporation, most of the major Raman bands shift towards lower energy (lower frequency) side, and the intensity of most of the Raman bands (111, 118, 134, 154, 308, 368, 496 and 629 cm^{-1}) decreases. While the intensities of the vibrational modes at 154 and 630 cm^{-1} decrease gradually to disappear at high Sn contents, there appeared three additional bands at about 174, 217 and 603 cm^{-1} for the sample prepared with 15 wt% nominal Sn content. The band at 174 cm^{-1} corresponds to Sn–O vibrations of ITO [39], while the two bands at 217 and 603 cm^{-1} correspond to IR-active modes of indium oxide [43], which become Raman active due to structural changes introduced by disorder and size reduction induced by Sn incorporation in In_2O_3 lattice [44]. The intensity variation and red shift of the 134, 308 and 368 cm^{-1} bands can be followed clearly from Fig. 10. The gradual decrease of intensity and increased FWHM (full width at half maximum) of the main Raman bands (Table 2) are the indication of lattice deformation due to Sn incorporation. As the ionic radius (0.69 Å) of tin (Sn^{4+}) is smaller than the ionic radius (0.80 Å) of indium (In^{3+}), incorporation of

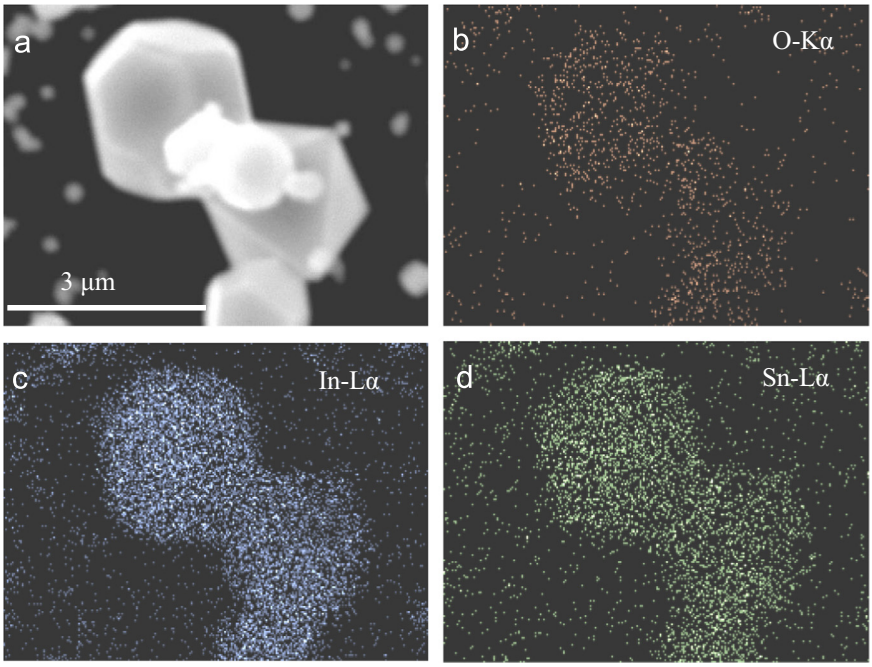

Fig. 5. (a) SEM image of 5 wt% (nominal) Sn-doped In_2O_3 sample, and its EDS elemental maps for (b) O-Kα, (c) In-Lα, and (d) Sn-Lα.

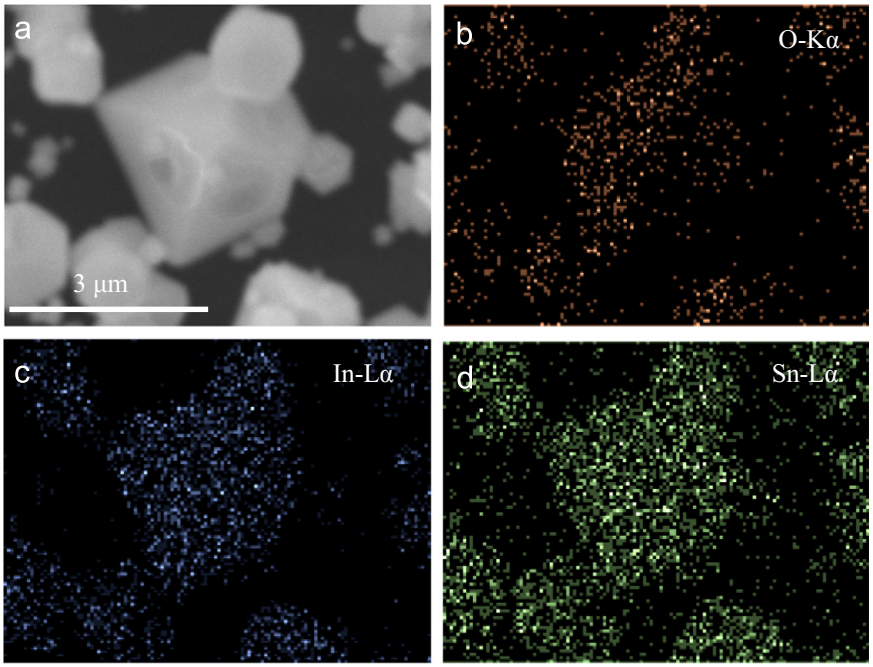

Fig. 6. (a) SEM image of 10 wt% (nominal) Sn-doped In_2O_3 sample, and its EDS elemental maps for (b) O-Kα, (c) In-Lα, and (d) Sn-Lα.

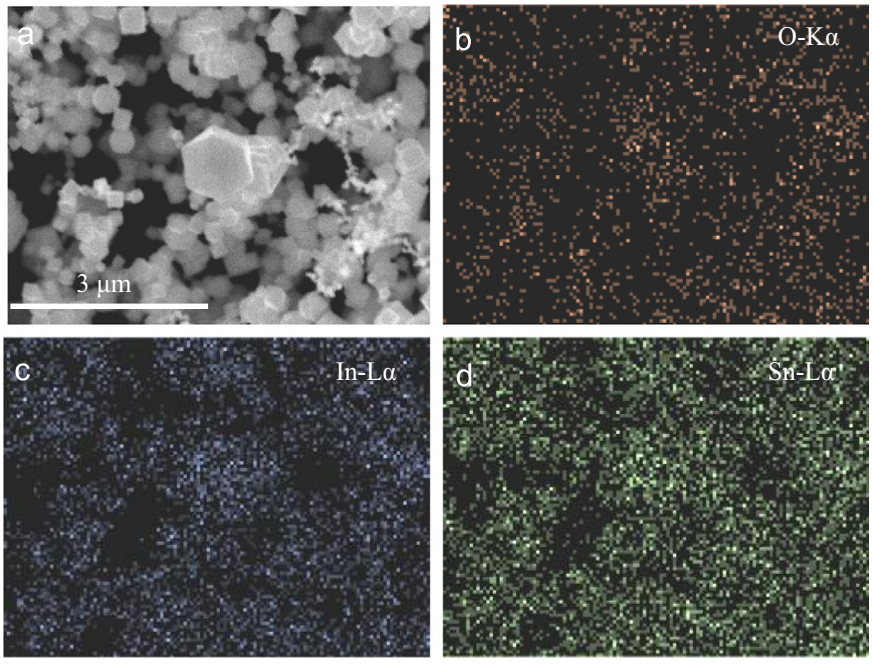

Fig. 7. (a) SEM image of 15 wt% Sn-doped In_2O_3 sample, and its EDS elemental maps for (b) O-Kα, (c) In-Lα, and (d) Sn-Lα.

Sn^{4+} ions through In^{3+} substitution is expected to cause a red shift of the 308 cm^{-1} and 368 cm^{-1} vibrational modes associated to In–O bonds in Raman spectra, due to a decrease in bonding energy [37]. Besides, Sn incorporation in In_2O_3 is seen to cause lattice distortion, increasing the FWHM of the Raman bands, affecting its local periodicity. The higher oxygen content in the micro-/nanoparticles estimated from their EDS analysis is probably due to the incorporation of O^{2-} ions into the lattice [26] in the growth process. The oxygen ions will remain at the interstitial sites of the lattice after filling up some or most of the existing oxygen vacancies. Thus, the lattice distortion is mainly caused by the interstitial oxygen ions as they occupy oxygen vacancy (V_O) sites, which are generally empty in pure In_2O_3 [45] and the content of oxygen increases with the increase of Sn content [46]. Although, these interstitial anions partially balance the extra charge of Sn^{4+} ions, they affect the inter-atomic distance, inducing distortion in In/Sn–O octahedron [26].

Optical absorption spectra of the doped and undoped nanostructures were recorded in the UV–vis spectral region dispersing them in ethanol. The absorption coefficient of the samples at different wavelengths was estimated utilizing the relation [47]:

$$\alpha = \frac{2303A\rho}{lC}, \tag{1}$$

where A is the absorbance of the sample; ρ is its density; C is the concentration of the sample in solution; and l is the optical path

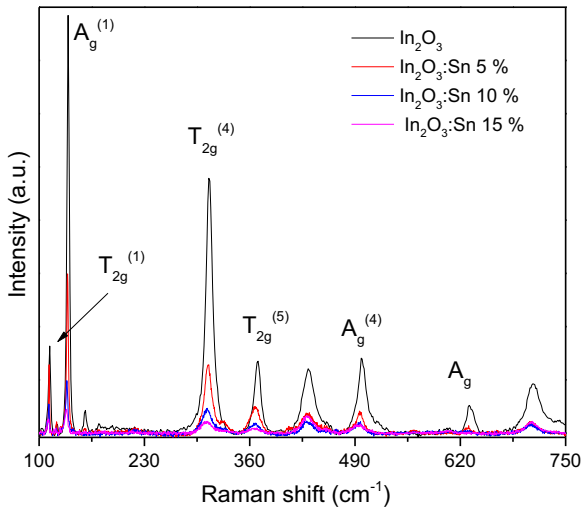

Fig. 8. Raman shifts in the undoped and Sn-doped In_2O_3 samples with different Sn contents.

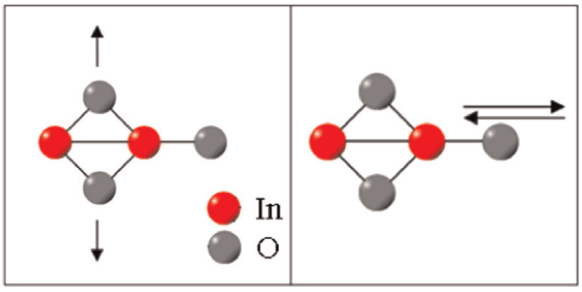

Fig. 9. Stretching vibrations of the rhombus (left) and terminal (right) oxygen atoms in In_2O_3 lattice, producing 119 and 429 cm^{-1} vibrational modes in their Raman spectrum.

length. The optical band gap energies of the samples for direct transition were estimated using the relation [48]:

$$(\alpha h\nu)^2 = A(E_g - h\nu), \tag{2}$$

where A is the constant, E_g is the band gap energy and $h\nu$ is the energy of incident radiation. Fig. 11 presents the $(\alpha h\nu)^2$ vs $h\nu$ plots for the In_2O_3 structures containing different Sn contents. The estimated band gap energy values were 3.60, 3.67, 3.83 and 3.96 eV for the undoped, nominal 5.0%, 10.0%, and 15.0% Sn-doped samples (Fig. 11), respectively, indicating a gradual increase with the increase of Sn content. According to the Burstein–Moss model, in an n-type semiconductor, the direct transitions are not the minimal separation of valence and conduction bands. Instead, the direct transitions are the transitions between the valence band and E_m, where E_m is the unoccupied lowest energy level at the bottom of the conduction band, which can be expressed as [49]:

$$E_m = (h^2/8\pi^2 m^*)(3\pi^2 n)^{2/3}, \tag{3}$$

where m^* and n are the effective mass of the electron and the carrier density, respectively [50]. Therefore, when the carrier density increases, the energy needed for a direct transition increases. However, for doping at high concentrations, this effect could be masked due to the formation of SnO, Sn_2O and Sn_4O_2 complexes, which act as carrier traps instead of electron donors [51]. The filling up of low energy states in the conduction band by the electrons of doped atoms, and the excited electrons from the valence band must have energy equal or higher than $E_0 = E_g + E_m$ to give an electronic transition. In the present case, while the optical band gap energy of the In_2O_3 samples increased by 0.18 eV on 5 wt% Sn (nominal) doping, it increase by further 0.27 eV on incorporating 15 wt% Sn (nominal). As can be seen from Table 1, the effective increase of Sn content in the latter case is very small compared to the former, which indicates that the incorporated Sn does not form any secondary oxide phase such as SnO, Sn_2O or Sn_4O_2.

CL measurements were performed on undoped and Sn-doped In_2O_3 samples at room temperature. All the samples revealed a broad CL emission in the visible spectral region associated to defects in In_2O_3 and relatively weaker emission in ultraviolet region. On Sn incorporation, while the intensity of the visible emission decreased, both the intensity and broadness of UV emission increased (Fig. 12).

In Fig. 13, room temperature (300 K) CL spectra of the samples along with their Gaussian deconvoluted components are presented separately. The CL spectrum of the undoped sample (Fig. 13 (a)) revealed a broad emission band centered around 2.21 eV, which on deconvolution resulted three component bands peaked around 1.93 eV (orange band), 2.24 eV (green band) and 2.91 eV (blue band). Although the appearance of orange band in the CL and PL spectra of In_2O_3 has been observed frequently [52, 53], its origin still remained unclear. Frequently, this band has been attributed to oxygen vacancies [54]. However, Kumar et al. [55] have associated

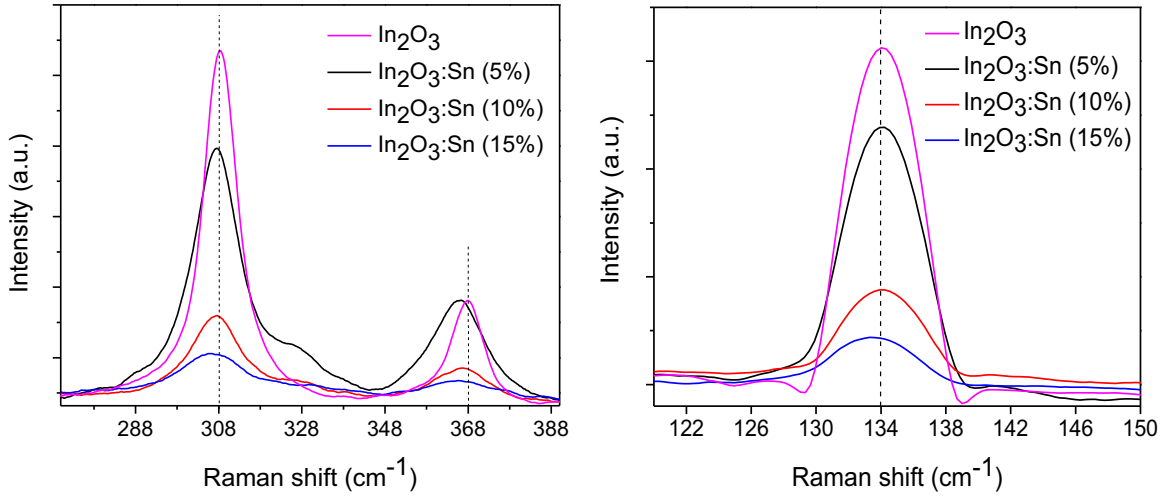

Fig. 10. Raman bands of Sn-doped In_2O_3 in the (a) 270–390 cm^{-1} and (b) 120–150 cm^{-1} spectral range, showing their lower energy shifts and intensity reduction due to Sn incorporation.

Table 2
Position of the principal Raman bands and their FWHM (in parenthesis) in the undoped and Sn-doped In_2O_3 particles.

Position and FWHM (cm^{-1}) of Raman modes						
Sample	T_g	A_g	T_g	T_g	T_g	A_g
In_2O_3	112.1 (3.7)	134.7 (3.6)	308.5 (9.8)	369.2 (9.6)	431.2 (18.2)	496.6 (12.8)
In_2O_3:Sn (5%)	109.6 (1.8)	132.5 (3.2)	305.4 (14.4)	362.6 (19.1)	429.71 (26.8)	493.1 (16.0)
In_2O_3:Sn (10%)	109.9 (1.8)	132.2 (3.3)	304.4 (15.2)	363.2 (19.1)	430.3 (17.8)	492.5 (20.6)
In_2O_3:Sn (15%)	109.6 (3.5)	131.9 (4.5)	305.4 (10.4)	367.24 (16.9)	428.48 (19.3)	494.3 (8.8)

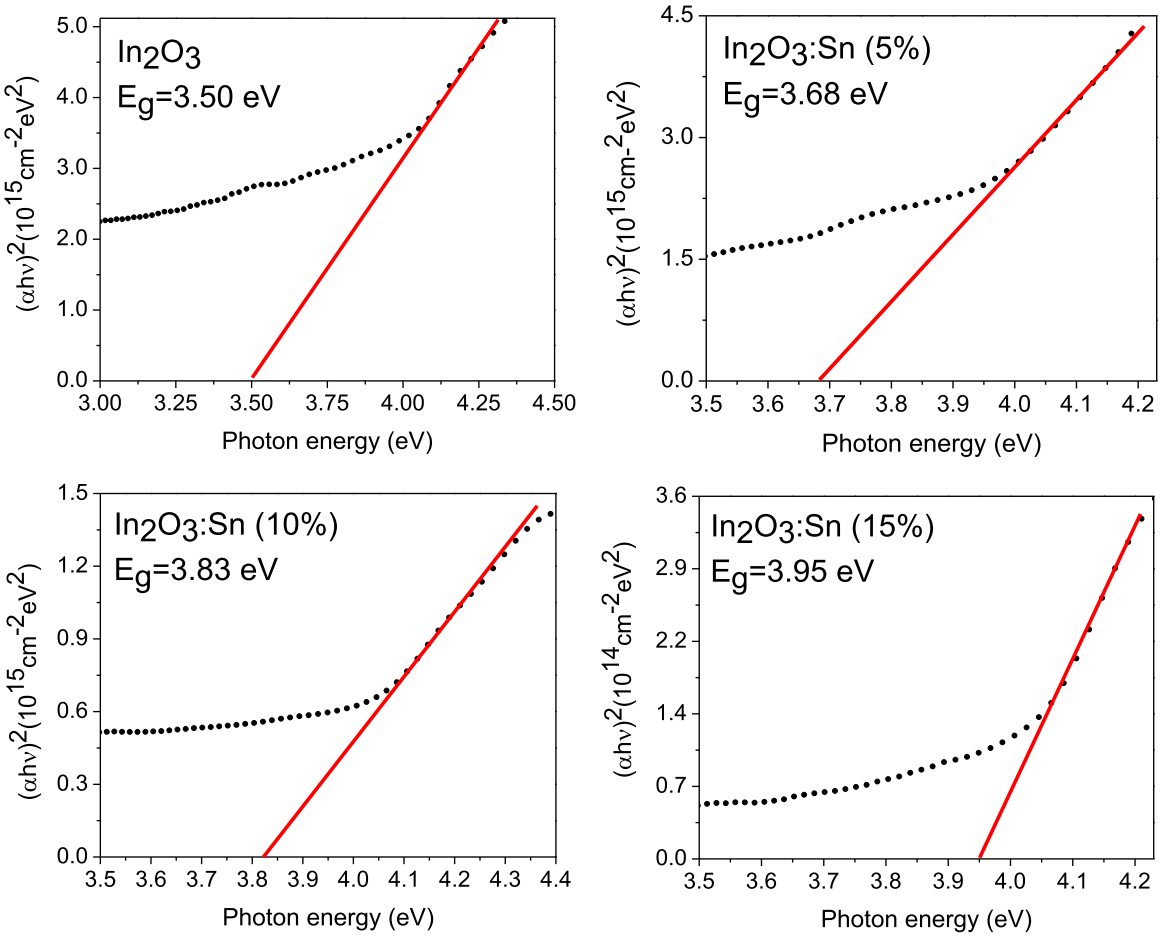

Fig. 11. $(\alpha h\nu)^2$ vs $h\nu$ plots and bandgap energy estimation of undoped and Sn-doped In_2O_3 nanoparticles for direct transition.

this emission band to the indium interstitial In_i^{3+} sites, instead of oxygen vacancies. The emission around 2.24 eV has been associated to point defects generated by oxygen excess, such as interstitial oxygen (O_i), indium vacancies (V_{In}) or antisite oxygen (O_{In}) in In_2O_3 [29]. As can be seen from Fig. 13(b) and(c), on Sn incorporation, there appeared two new emission bands around 2.51 eV (green–blue) and 3.32 eV (violet) in the CL spectra of In_2O_3 samples. Appearance of these higher energy bands has been associated to the defects introduced by Sn doping in In_2O_3 lattice [56]. However, on increasing Sn content (Fig. 13(c)), the relative intensity of the 2.24 eV band decreased. As has been discussed earlier, due to the valance charge difference between Sn^{4+} and In^{3+} ions, O^{2-} ions must incorporate into In_2O_3 lattice to balance the charge in the lattice of Sn-doped In_2O_3. The excess oxygen ions occupy V_O sites (oxygen vacancies), which are typically empty in pure In_2O_3 [45]. Incorporation of O^{2-} ions causes the reduction of the 2.24 eV emission band intensity and enhances the intensity of 2.51 and 3.32 eV bands. The intensity ratio of the green and blue emissions (I_g/I_b) estimated for the In_2O_3:Sn samples containing nominal 0, 5, 10 and 15 wt% of Sn were 20.80, 3.19, 0.68 and 0.46, respectively, revealing a gradual decrease on the increase of Sn content. Such a variation of emission intensity has also been reported for Sn-doped indium oxide nanowires [57], where the intensity of blue emission increases on increasing Sn content. On the other hand, a defect-related blue emission of 2.58 eV close to our designated green–blue emission, has been observed frequently in SnO_2 nanostructures [58], which is attributed to the formation of surface point defects in this semiconductor by several authors [58,59]. Generation of such point-defects in the vicinity of the Sn impurity is probably responsible for the gradual increase of blue emission in In_2O_3 samples on increasing Sn content (Fig. 13).

The low temperature (100 K) CL spectra of the undoped and Sn-doped samples (Fig. 14) reveled all the emission bands observed at room temperature, with noticeable change in their relative

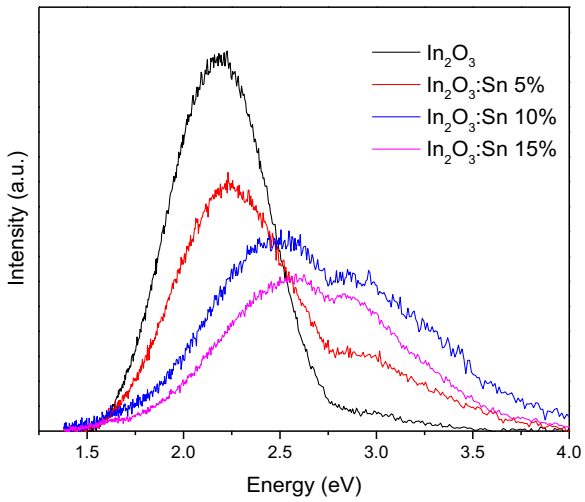

Fig. 12. Room temperature CL spectra of undoped and Sn-doped In_2O_3 nanoparticles.

intensities. The change is more evident for the case of undoped sample, where the relative intensity of the orange emission is much higher to the intensity of green emission. In general, the intensity ratio of the green and blue emissions (I_g/I_b) decreases with Sn doping, as observed for the CL emissions at 300 K. However, the relative intensity of blue emission (2.91 eV) in the 100 K CL spectrum of 5 wt% Sn doped sample is very high with respect to all the other Sn-doped samples, which needs a further investigation to be explained.

4. Conclusions

In summary, using vapor–solid growth process, we could fabricate octahedral shaped In_2O_3 micro-/nanostructures successfully. Due to limited solubility of Sn in In_2O_3, even with about 15 wt% of Sn in the precursor, only about 0.6 at% of Sn could be incorporated in the micro-/nanostructures. Incorporation of Sn in In_2O_3 micro-/nanostructures severely affects their morphology and defect distributions. Due to the difference in valence charge between Sn^{4+} and In^{3+} ions, substitution of the former by the later ions incorporate extra O^{2-} ions at interstitial sites of In_2O_3 lattice, reducing the concentration of oxygen vacancies (V_O). While Sn incorporation causes a gradual increase in the band gap energy of In_2O_3, it reduces the relative intensity of the green emission and enhances the relative intensity of blue emission. Therefore, through controlled Sn doping, the emission behavior of In_2O_3 micro-/nanocrystals can be controlled.

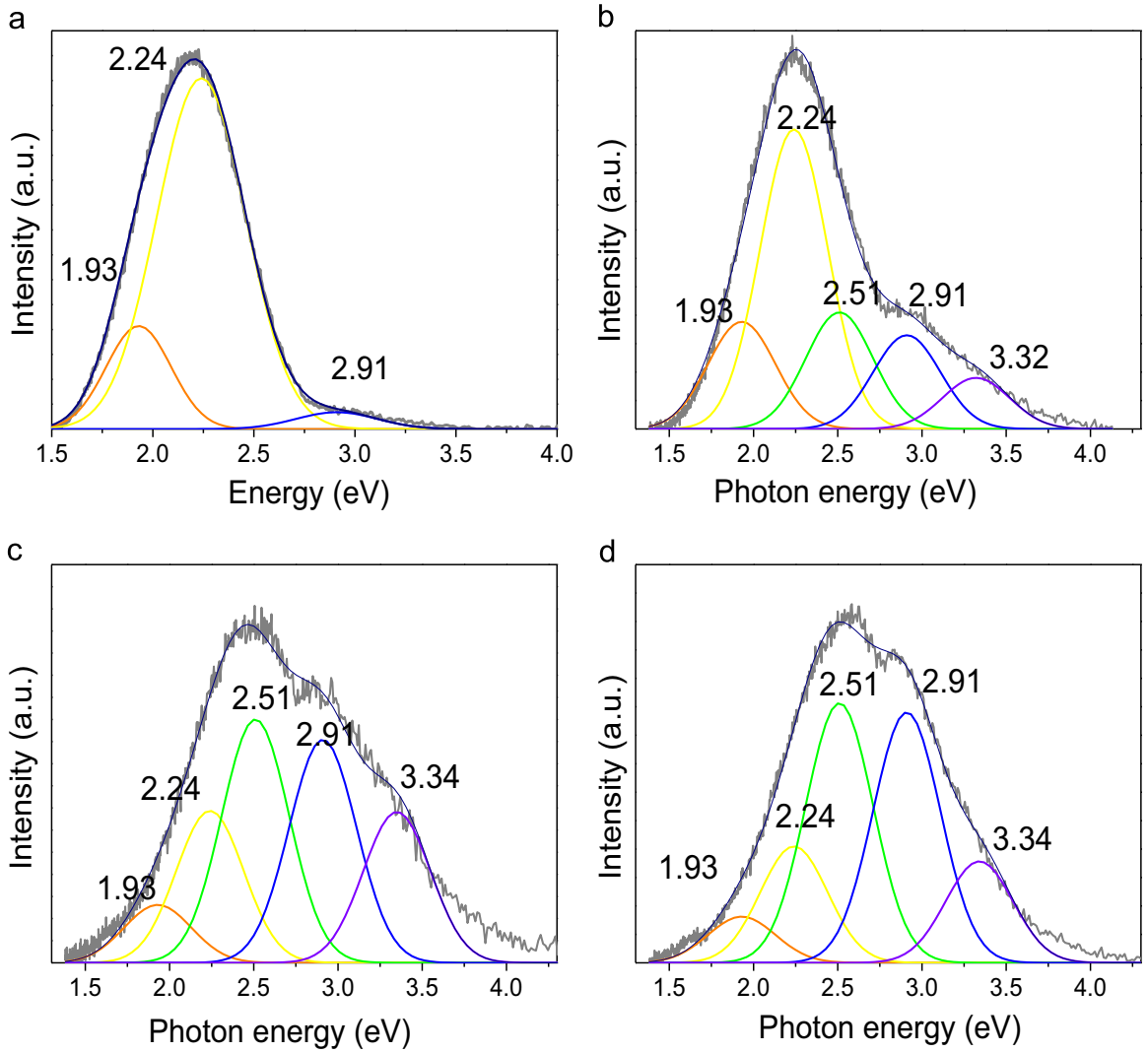

Fig. 13. Deconvoluted CL spectra of the (a) undoped, (b) 5 wt%, (c) 10 wt%, and (d) 15 wt% Sn-doped (nominal) In_2O_3 particles obtained at 300 K.

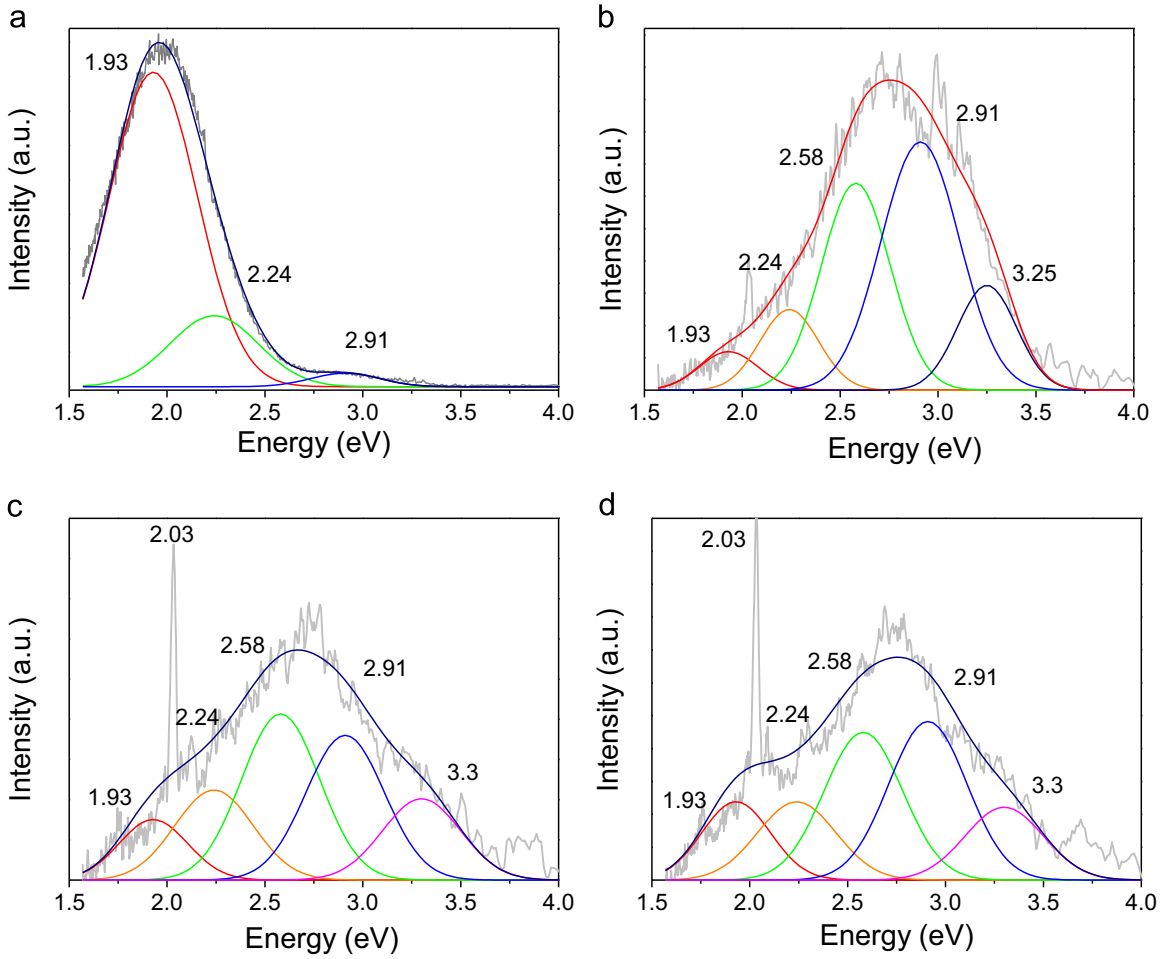

Fig. 14. Deconvoluted CL spectra of the (a) undoped (b) 5%, (c) 10% and (d) 15% Sn-doped (nominal) In_2O_3 particles obtained at 100 K.

Acknowledgments

The authors are thankful to CONACyT (Grants # CB-2010/161767 and CONACyT-DST # 163646), and VIEP-BUAP (Grant # VIEP/EXC/2015) for providing financial supports.

References

[1] X.B. Li, Y. Xie, M. Jing, G.X. Rong, Y.C. Tang, G.Z. Zhang, In_2O_3 hollow microspheres: synthesis from designed $In(OH)_3$ precursors and applications in gas sensors and photocatalysis, Langmuir 22 (2006) 9380–9385.
[2] M. Takeuchi, Y. Watanabe, S. Ozawa, Gas-sensitive properties of ultrafine In_2O_3 particle layers prepared by gas evaporation technique, Appl. Surf. Sci. 48 (1991) 526–529.
[3] C.H. Liang, G.W. Meng, Y. Lei, F. Phillipp, L.D. Zhang, Catalytic growth of semiconducting In_2O_3 nanofibers, Adv. Mater. 13 (2001) 1330–1333.
[4] C.G. Granqvist, Transparent conductive electrodes for electrochromic devices: a review, Appl. Phys. A: Solids Surf. 57 (1993) 19–24.
[5] I. Hamberg, C.G. Granqvist, Optical properties of transparent and heat-reflecting indium tin oxide films: the role of ionized impurity scattering, Appl. Phys. Lett. 44 (1984) 721–723.
[6] V.P. Reddy, A.V. Kumar, K. Swapna, K.R. Rao, Nano indium oxide as a recyclable catalyst for C–S cross-coupling of thiols with aryl halides under ligand free conditions, Org. Lett. 11 (2009) 1697–1700.
[7] S. Lin, X. Ye, First-principle insights into the catalytic role of indium oxide in methanol steam reforming, Chin. J. Catal. 34 (2013) 1855–1860.
[8] C. Li, D. Zhang, S. Han, X. Liu, T. Tang, C. Zhou, Diameter-controlled growth of single-crystalline In_2O_3 nanowires and their electronic properties, Adv. Mater. 15 (2003) 143–146.
[9] T. Bielz, H. Lorenz, P. Amann, B. Klotzer, S. Penner, Water–gas shift and formaldehyde reforming activity determined by defect chemistry of polycrystalline In_2O_3, J. Phys. Chem. C 115 (2011) 6622–6628.
[10] M. Kumar, V.N. Singh, B.R. Mehta, J.P. Singh, Tunable growth of indium oxide from nanoflute to metal-filled nanotubes, J. Phys. Chem. C 116 (2012) 5450–5455.
[11] O.N. Mryasov, A.J. Freeman, Electronic band structure of indium tin oxide and criteria for transparent conducting behavior, Phys. Rev. B 64 (2001) 233111-1–233111-3.
[12] C.L. Hsin, J.H. He, L.J. Chen, Modulation of photoemission spectra of In_2O_3 nanowires by the variation in Zn doping level, Appl. Phys. Lett. 88 (2006) 063111-1–063111-3.
[13] J.M. Phillips, R.J. Cava, G.A. Thomas, S.A. Carter, J. Kwo, T. Siegrist, J.J. Krajewski, J.H. Marshall, W.F. Peck Jr., D.H. Rapkine, Zinc–indium-oxide: a high conductivity transparent conducting oxide, Appl. Phys. Lett. 67 (1995) 2246–2248.
[14] W. Zhang, J. Jie, Z. He, S. Tao, X. Fan, Y. Zhou, G. Yuan, L. Luo, W. Zhang, C.-S. Lee, S.-T. Lee, Single zinc-doped indium oxide nanowire as driving transistor for organic light-emitting diode, Appl. Phys. Lett. 92 (2008) 153312-1–153312-3.
[15] C.C. Wu, C.I. Wu, J.C. Sturm, A. Kahn, Surface modification of indium tin oxide by plasma treatment: an effective method to improve the efficiency, brightness, and reliability of organic light emitting devices, Appl. Phys. Lett. 70 (1997) 1348–1350.
[16] N.G. Pramod, S.N. Pandey, P.P. Sahay, Sn-Doped In_2O_3 nanocrystalline thin films deposited by spray pyrolysis: microstructural, optical, electrical, and formaldehyde-sensing characteristics, J. Therm. Spray Technol. 22 (2013) 1035–1043.
[17] A. El Hichou, A. Kachouane, J.L. Bubendorff, M. Addou, J. Ebothe, M. Troyon, A. Bougrine, Effect of substrate temperature on electrical, structural, optical and cathodoluminescent properties of In_2O_3–Sn thin films prepared by spray pyrolysis, Thin Solid Films 458 (2004) 263–268.
[18] E. Comini, G. Fagila, G. Sberveglieri, Z. Pan, Z.L. Wang, Stable and highly sensitive gas sensors based on semiconducting oxide nanobelts, Appl. Phys. Lett. 81 (2002) 1869–1871.
[19] H. Jia, Y. Zhang, X. Chen, J. Shu, X. Luo, Z. Zhang, Efficient field emission from single crystalline indium oxide pyramids, Appl. Phys. Lett. 82 (2003) 4146–4148.
[20] N. Du, H. Zhang, B. Chen, X. Ma, Z. Liu, J. Wu, D. Yang, Porous indium oxide nanotubes: layer-by-layer assembly on carbon-nanotube templates and application for room-temperature NH_3 gas sensors, Adv. Mater. 19 (2007) 1641–1645.
[21] S.K. Chong, S.N. Azieani Azizan, K.W. Chan, H.-Q. Nguyen, W.S. Chiu, Z. Aspanut, C.F. Dee, S.A. Rahman, Structure deformation of indium oxide from nanoparticles into nanostructured polycrystalline films by in situ thermal

radiation treatment, Nanoscale Res. Lett. 8 (2013) 428–436.
[22] G. Korotcenkov, M. Nazarov, M.V. Zamoryanskaya, M. Ivanov, Cathodoluminescence emission study of nanocrystalline indium oxide films deposited by spray pyrolysis, Thin Solid Films 515 (2007) 8065–8071.
[23] C.Y. Wang, Y. Dai, J. Pezolt, B. Lu, T. Kups, V. Cimalla, O. Ambacher, Phase stabilization and phonon properties of single crystalline rhombohedral indium oxide, Cryst. Growth Des. 8 (2008) 1257–1260.
[24] H.J. Chun, Y.S. Choi, S.Y. Bae, H.C. Choi, J. Park, Single-crystalline gallium-doped indium oxide nanowires, Appl. Phys. Lett. 85 (2004) 461–463.
[25] H. Zhu, X. Wang, F. Yang, X. Yang, Template-free, surfactantless route to fabricate $In(OH)_3$ monocrystalline nanoarchitectures and their conversion to In_2O_3, Cryst. Growth Des. 8 (2008) 950–956.
[26] J. Ba, D.F. Rohlfing, A. Feldhaff, T. Brezesinski, I. Djerdj, M. Wark, M. Niederberger, Nonaqueous synthesis of uniform indium tin oxide nanocrystals and their electrical conductivity in dependence of the tin oxide concentration, Chem. Mater. 18 (2006) 2848–2854.
[27] W. Yin, J. Su, M. Cao, C. Ni, S.G. Cloutier, Z. Huang, X. Ma, L. Ren, C. Hu, B. Wei, $In(OH)_3$ and In_2O_3 micro/nanostructures: controllable NaOAc-assisted microemulsion synthesis and raman properties, J. Phys. Chem. C 113 (2009) 19493–19499.
[28] M.J. Zheng, L.D. Zhang, G.H. Li, X.Y. Zhang, X.F. Wang, Ordered indium-oxide nanowire arrays and their photoluminescence properties, Appl. Phys. Lett. 79 (2001) 839–841.
[29] M. Mazzera, M. Zha, D. Calestani, A. Zappettini, L. Lazzarini, G. Salviati, L. Zanotti, Low-temperature In_2O_3 nanowire luminescence properties as a function of oxidizing thermal treatments, Nanotechnology 18 (2007) 355707–355713.
[30] X. Wu, Y. Wang, B. Yang, Effects of Sn doping on the morphology, structure, and electrical property of In_2O_3 nanofiber networks, Appl. Phys. A 117 (2014) 781–786.
[31] P. Guha, S. Kar, S. Chaudhuri, Direct synthesis of single crystalline In_2O_3 nanopyramids and nanocolumns and their photoluminescence properties, Appl. Phys. Lett. 85 (2004) 3851–3853.
[32] Y. Hao, G.W. Meng, C.H. Ye, L.D. Zhang, Controlled synthesis of In_2O_3 octahedrons and nanowires, Cryst. Growth Des. 5 (2005) 1617–1621.
[33] A. Reindl, M. Mahajeri, J. Hanft, W. Peukert, The influence of dispersing and stabilizing of indium tin oxide nanoparticles upon the characteristic properties of thin films, Thin Solid Films 517 (2009) 1624–1629.
[34] X.B. Jiang, M. Jiang, M. Zhao, Thermodynamic understanding of phase transitions of In_2O_3 nanocrystals, Chem. Phys. Lett. 563 (2013) 76–79.
[35] Z.L. Wang, Transmission electron microscopy of shape-controlled nanocrystals and their assemblies, J. Phys. Chem. B 104 (2000) 1153–1175.
[36] C. Herring, Some theorems on the free energies of crystal surfaces, Phys. Rev. 82 (1951) 87–93.
[37] R.E. Honig, Vapor pressure data for the more common elements, RCA Rev. 18 (1957) 195–204.
[38] P. Gali, F.-L. Kuo, N. Shepherd, U. Philipose, Role of oxygen vacancies in visible emission and transport properties of indium oxide nanowires, Semicond. Sci. Technol. 27 (2012) 015015-1–015015-5.
[39] O.M. Berengue, A.D. Rodrigues, C.J. Dalmaschio, A.J.C. Lanfredi, E.R. Leite, A. J. Chiquito, Structural characterization of indium oxide nanostructures: a Raman analysis, J. Phys. D: Appl. Phys. 43 (2010) 045401-1–045401-4.
[40] M.-J. Xu, Y. Ni, Z.-Q. Li, S.-L. Wang, X.-H. Liu, X.-M. Dou, Structural, electronic and vibrational properties of indium oxide clusters, Chin. Phys. B 20 (2011) 063101-1–063101-9.
[41] W.B. White, V.G. Keramidas, Vibrational spectra of oxides with the C-type rare earth oxide structure, Spectrochim. Acta A 28 (1972) 501–509.
[42] D.-W. Kim, I.-S. Hwang, S.J. Kwon, G.-Y. Kang, K.-S. Park, Y.-J. Choi, K.-J. Choi, J.-G. Park, Highly conductive coaxial SnO_2–In_2O_3 heterostructured nanowires for Li ion battery electrodes, Nano Lett. 7 (2007) 3041–3045.
[43] A. Singhal, S.N. Achary, J. Manjanna, O.D. Jayakumar, R.M. Kadam, A.K. Tyagi, Colloidal Fe-Doped indium oxide nanoparticles: facile synthesis, structural, and magnetic properties, J. Phys. Chem. C 113 (2009) 3600–3606.
[44] J. Gao, R. Chen, D.H. Li, L. Jiang, J.C. Ye, X.C. Ma, X.D. Chen, Q.H. Xiong, H.D. Sun, T. Wu, UV light emitting transparent conducting tin-doped indium oxide (ITO) nanowires, Nanotechnology 22 (2011) 195706-1–195706-10.
[45] C. Li, W. Fan, B. Lei, D. Zhang, S. Han, T. Tang, X. Liu, Z. Liu, S. Asano, M. Meyyappan, J. Han, C. Zhou, Multilevel memory based on molecular devices, Appl. Phys. Lett. 84 (2004) 1949–1951.
[46] M. Quaas, C. Eggs, H. Wulff, Structural studies of ITO thin films with the Rietveld method, Thin Solid Films 332 (1998) 277–281.
[47] F. Gu, S.F. Wang, M.K. Lü, G.J. Zhou, D. Xu, D.R. Yuan, Photoluminescence properties of SnO_2 nanoparticles synthesized by sol–gel method, J. Phys. Chem. B 108 (2004) 8119–8123.
[48] S. Maensiri, P. Laokul, V. Promarak, Synthesis and optical properties of nanocrystalline ZnO powders by a simple method using zinc acetate dihydrate and poly(vinyl pyrrolidone), J. Cryst. Growth 289 (2006) 102–106.
[49] E. Burstein, Anomalous optical absorption limit in InSb, Phys. Rev. 93 (1954) 632–633.
[50] T.S. Moss, The interpretation of the properties of indium antimonide, Proc. Phys. Soc. B 67 (1954) 775–782.
[51] H. Kim, C.M. Gilmore, A. Piqué, J.S. Horwitz, H. Mattoussi, H. Murata, Z. H. Kafafi, D.B. Chrisey, Electrical, optical, and structural properties of indium–tin-oxide thin films for organic light-emitting devices, J. Appl. Phys. 86 (1999) 6451–6461.
[52] M. Herrera, A. Cremades, D. Maestre, J. Piqueras, Growth and characterization of Mn-doped In_2O_3 nanowires and terraced microstructures, Acta Mater. 75 (2014) 51–59.
[53] L.C. Ten, Y.-Y. Hsieh, Defect induced ferromagnetism in undoped In_2O_3 nanowires, Mater. Res. Bull. 60 (2014) 690–694.
[54] T. Gao, T. Wang, Catalytic growth of In_2O_3 nanobelts by vapor transport, J. Cryst. Growth 290 (2006) 660–664.
[55] M. Kumar, V.N. Singh, F. Singh, K.V. Lakshmi, B.R. Mehta, J.P. Singh, On the origin of photoluminescence in indium oxide octahedron structures, Appl. Phys. Lett. 92 (2008) 171907-1–171907-3.
[56] Y.-C. Liang, H. Zhong, Self-catalytic crystal growth, formation mechanism, and optical properties of indium tin oxide nanostructures, Nanoscale Res. Lett. 8 (2013) 358–367.
[57] C.H. Kuo, P.Y. Yang, W.-H. Chen, S.J. Lin, Synthesis of transparent metallic Sn-doped In_2O_3 nanowires: effects of doping concentration on photoelectric properties, Phys. Status Solidi A 211 (2014) 488–493.
[58] M. Herrera, D. Maestre, A. Cremades, J. Piqueras, Growth and characterization of Mn doped SnO_2 nanowires, nanobelts, and microplates, J. Phys. Chem. C 117 (2013) 8997–9003.
[59] S. Kim, T. Lim, S. Ju, Fabrication of reliable semiconductor nanowires by controlling crystalline structure, Nanotechnology 22 (2011) 305704-1–305704-6.